Computer Physics Communications 311 (2025) 109573

Contents lists available at ScienceDirect

Computer Physics Communications

journal homepage: www.elsevier.com/locate/cpc

Computational Physics

Derivative transfer matrix method: Machine precision calculation of electron structure and interface phonon dispersion in semiconductor heterostructures

N. Stanojević [a,b,*], A. Demić [c], N. Vuković [a], P. Dean [c], Z. Ikonić [c], D. Indjin [c], J. Radovanović [a]

[a] School of Electrical Engineering, University of Belgrade, Bulevar kralja Aleksandra 73, Belgrade, 11120, Serbia
[b] Vlatacom Institute of High Technologies, Bulevar Milutina Milankovica 5, Belgrade, 11070, Serbia
[c] School of Electronic and Electrical Engineering, University of Leeds, Woodhouse Lane, Leeds, LS2 9JT, UK

ARTICLE INFO

The review of this paper was arranged by Prof. David W.Walker

Dataset link: https://doi.org/10.5518/1639

Keywords:
Transfer matrix method
Machine precision
Electron structure
Interface phonon
Terahertz quantum cascade laser

ABSTRACT

We develop a machine precision transfer matrix method that can be used for a wide range of ordinary differential equations and eigenvalue problems. One of the major drawbacks of transfer matrix approaches is the requirement to sweep parameters in a shooting-like manner, thus lacking in precision in comparison to finite difference methods. We resolve this by finding the zero of the analytically calculated first derivative of the transfer matrix. This allows us to outperform the finite difference approach and compute eigenvalues with high precision and linear numerical complexity. We test the developed model in the following scenarios in semiconductor quantum heterostructures: standard Schrödinger equation under effective mass approximation with parabolic subbands, with two-band nonparabolicity, a 4th order Schrödigner equation that accounts for nonparabolic subbands using the 14 **k**·**p** approach and calculation of the interface phonon modes dispersion relations and the mode profiles. We show that the developed derivative transfer matrix method outperforms the finite difference method by being able to handle higher spatial resolution and having better time performance. The numerical implementation of our models is available as an open-source package in MATLAB version that can be found on https://github.com/AcaDemicNanoLab/dTMM_Schrodinger.

1. Introduction

The transfer matrix method (TMM) is a widely used numerical method for solving ordinary differential equations (ODE) first introduced as a mathematical technique in statistical mechanics [1]. The TMM has found many applications such as the calculation of propagation characteristics in planar waveguides [2,3], the investigation of spontaneous emission in a DFB-laser [4,5], analysis of acoustic waves in multilayered structures [6–8], solving the photonic band structure in photonic crystals [9–11], as well as the investigation of bound and scattering states in metal–oxide–semiconductor (MOS) structures or quantum-well heterostructures [12–16].

The TMM approach offers an intuitive way of solving ODEs due to its ability to sew analytical solutions across the numerical grid. However, for eigenvalue problems, such as the calculation of electronic structure, two issues arise: the elements in the total transfer matrix do not have the same order of magnitude for eigenvalue solutions and the eigenvalue search is typically performed through a shooting-like approach [17]. The first issue is resolved by seeking minimal or maximal values of TMM elements instead, while the second issue has not been addressed in the literature so far to the best of our knowledge. In this work, we introduce a compact algorithm that calculates the first derivative of the transfer matrix with linear numerical complexity. This approach allows us to avoid a shooting-like search for eigenvalues and employ incremental search zero-finding algorithms for the first derivative of the transfer matrix which typically converge quickly. The theoretical framework of our derivative transfer matrix method (dTMM) is presented in Section 2. Recently there have been some applications of the derivative of the transfer matrix for the sensitivity analysis for multibody systems [18,19], as well as for the analysis of multiple natural frequencies for

* Corresponding author at: School of Electrical Engineering, University of Belgrade, Bulevar kralja Aleksandra 73, Belgrade, 11120, Serbia.
E-mail addresses: novakstanojevic1@gmail.com, novak.stanojevic@vlatacom.com (N. Stanojević).

https://doi.org/10.1016/j.cpc.2025.109573
Received 4 July 2024; Received in revised form 5 February 2025; Accepted 28 February 2025
Available online 4 March 2025

the vibration of a symmetric mechanical system [20]. We note that our approach extends beyond eigenvalue problems as our algorithm enables seeking the first derivative of any parameter that affects the total transfer matrix within the TMM framework. In our analysis, we study two ODEs in which TMM has been applied extensively: calculation of the electronic structure of devices based on multiple quantum well (MQW) semiconductor superlattice and calculation of interface phonon modes in semiconductor heterostructures via the dielectric continuum model (DCM).

Quantum Cascade Lasers (QCLs) [21–24] are MQW devices that employ hundreds of alternating semiconductor layers to tailor the electronic structure for unipolar laser emission. This has allowed QCLs to generate sources beyond the limits of the material bandgap in traditional semiconductor lasers. QCLs emit from mid-infrared to the far-infrared part of the spectrum, spanning energy separations on a scale of hundreds of meV to only several meV. This has led to increasing number of applications in imaging, medical diagnostics, and chemical sensing [25–32].

The calculation of QCL electronic structures requires the solving of the Schrödinger equation, usually within the electron effective mass formalism. The solutions are Bloch waves representing quasibound quantum subbands that can be exploited for the lasing process. The subbands have parabolic dispersion in k space, but depending on the underlying material systems and crystal structure the solutions may deviate from parabolic dispersion and require treatment of nonparabolicity during the calculation of the electronic structure. These effects are essential in semiconductor structures with small bandgaps, MQW systems that comprise narrow energy spacing between the subbands and MQW systems that exploit high-energy subbands.

There are several approaches to the calculation of nonparabolicity effects in the conduction band, the most common is the two-band Kane model that takes into account the interaction of the conduction band and the light-hole valence band [33–36]. A more complex treatment takes into account three bands or more such as in the work by Ekenberg [37] that treats 14 bands resulting in the Schrödinger equation of the 4^{th} order.

In Section 3 we apply our dTMM to calculate the parabolic and two-band nonparabolic electron structure of terahertz-frequency (THz) QCLs grown in different material combinations. We validate our model by comparing with a finite difference method (FDM) [38] and analyse an exemplary structure that is particularly sensitive to numerical precision of calculated eigenvalues and for which the standard TMM approach may cause diverging solutions.

In Section 4 we apply the dTMM to the calculation of the nonparabolic electron structure of QCLs within the 14 $\mathbf{k}\cdot\mathbf{p}$ model from [37,39]. We investigate the effect of nonparabolicity on the electron structure of the conduction band, and compare the results with the two band nonparabolic model.

In Section 5 we analyse the numerical performance of both the dTMM and the FDM. We compare the CPU-time performance as well as the convergence of calculated ground and lasing level states of these numerical solvers versus the spatial resolution of the numerical grid applied to an exemplary QCL.

The optical-phonon-assisted electron transitions play an important role in QCLs. The spacial confinement in heterostructues affects both the semiconductor electron structure, and the acoustic and optical-phonon modes, which further affect the interaction between electrons and these phonon modes. As a result of this confinement, interface and confined phonon modes are formed. A standard way of calculating the dispersion relations and electrostatic phonon potentials of interface modes is by using the TMM [40].

In Section 6 we show how the dTMM can be used for the calculation of the dispersion relations of localised interface phonon modes in heterostructures and the calculation of the electrostatic potential of each mode within the DCM formalism.

We note that all applications of dTMM approach treated in this paper are accompanied by the corresponding numerical package. Our software is released in MATLAB version which can be found on https://github.com/AcaDemicNanoLab/dTMM_Schrodinger.

2. Derivative transfer matrix method

The TMM is a general numerical method that can be used for a wide range of problems that deal with ODEs. Its requirement is that the total system can be broken into a sequence of subsystems that interact only with adjacent subsystems. Another requirement is that for each of these adjacent subsystems analytical solutions are available.

The analytical solutions of a ODE x_i and x_{i+1} for two adjacent subsystems are k-dimensional vectors consisting of the eigenstates of the equation of the i-th and the $i+1$-th subsystem respectively, hence k is typically equal to the order of ODE equation. The transfer matrix M_i is a $k \times k$ matrix that describes the transition between the i-th and the $i+1$-th subsystem, which can be written as:

$$x_{i+1} = M_i x_i \tag{1}$$

If we apply Eq. (1) recursively across the entire grid and link the starting and the ending subsystem, the solution of the ODE is:

$$x_{N_z+1} = M_{N_z} M_{N_z-1} .. M_2 M_1 x_1 = M x_1 \tag{2}$$

where M is the total transfer matrix of the system.

Depending on the application, m_{ij} elements (or their combinations) in M matrix need to satisfy particular conditions, typically for which certain boundary conditions must be satisfied, and that imposes a condition for the solutions of the first x_1 and the last subsystem x_{N_z+1}. This usually requires us to seek the condition that some m_{ij} (or their combination) element is zero, minimal or maximal.

In eigenvalue ODEs, such as the Schrödinger equation, which is used for the calculation of the electronic structure, the TMM requires us to seek zeroes or extrema of $m_{ij}(E)$ dependence, so that a particular eigenvalue E represents the solution of the ODE. In numerical calculations m_{ij} is often a complex number, so instead of finding the zero of m_{ij}, the minimum of the modulus $|m_{ij}|$ is found and the eigenvalue that corresponds to this condition is taken as the energy of the subband state.

The challenge that arises is that the eigenvalue grid needs to be traversed with usually equidistant step dE, thus the value of dE would dictate the numerical precision of the calculated eigenvalues. This is one of the key drawbacks of the standard TMM approach, as the numerical cost for achieving machine precision in a "shooting-like" sweep of potential eigenvalues is extremely high given that we typically need to cover eigenvalue range of several hundreds of meV with $dE \approx 10^{-16}$ meV spacing. We note that Schrödigner equation can be solved with a FDM that results in a corresponding system matrix whose eigenvalues are at the same time required solutions and these inherently have machine precision.

The standard TMM approach may be accelerated by using the adaptive mesh approach [39]. For instance, if we perform an eigenvalue sweep with a coarse dE step, we will obtain a set of potential eigenvalue candidates, and then we can repeat the TMM approach in a narrow grid around each candidate. If we repeat this process several times, we may achieve the same precision as the FDM approach. However, the drawback of this approach is that we need to evaluate the function $m_{ij}(E)$ in each step, and given that $m_{ij}(E)$ is determined from analytical subsystems that are discretized on a spatial grid of size N_z, this is still a very costly algorithm.

The standard TMM approach and its acceleration through the adaptive mesh have been a trademark of the TMM formalism in the literature, with a remark that the TMM cannot achieve machine precision for eigenvalue problems efficiently as FDM approaches. To the best of our knowledge, there was no attempt to exploit the semi-analytic nature of TMM and calculate its first derivative. This would enable us to find extrema of $|m_{ij}(E)|$ elements through a range of zero finding algorithms,

savings us unnecessary calculations of $|m_{ij}(E)|$ in adaptive mesh grids and the only potential drawback would be the algorithmic cost of calculating the derivative of the transfer matrix. In this work, we show that the numerical complexity of calculating $\frac{d|m_{ij}(E)|}{dE}$ is linear.

The total transfer matrix is given in Eq. (2), and since this is a composite matrix product of matrices in Eq. (1), the first derivative of total transfer matrix is:

$$\frac{dM}{dE} = \frac{d(M_{N_z}M_{N_z-1}..M_2M_1)}{dE} = \frac{dM_{N_z}}{dE}M_{N_z-1}..M_2M_1 + M_{N_z}\frac{dM_{N_z-1}}{dE}..M_2M_1... + M_{N_z}M_{N_z-1}..\frac{dM_2}{dE}M_1 + M_{N_z}M_{N_z-1}..M_2\frac{dM_1}{dE} \quad (3)$$

The sum in Eq. (3) contains N_z terms, each of which is a product of N_z parts, where N_z is the total number of subsystems on a spatial grid on which we are applying the TMM. In order to avoid the $\mathcal{O}(N_z^2)$ numerical complexity in calculating the sum in Eq. (3), we can first calculate the arrays of the left and right cumulative products, both of which have the length N_z. In this manner all of the products are calculated only once, and placed into the appropriate positions in these two arrays that are later ready for use when calculating the terms within the derivative of the total transfer matrix in Eq. (3). The elements of the arrays of cumulative products can be written as:

$$\begin{aligned} &M^c_{\text{left}}(i) = M_iM_{i-1}...M_2M_1 = M_iM^c_{\text{left}}(i-1) \\ &M^c_{\text{right}}(i) = M_{N_z}M_{N_z-1}...M_{i+1}M_i = M^c_{\text{right}}(i+1)M_i \\ &M^c_{\text{left}}(1) = M_1 \text{ and } M^c_{\text{right}}(N_z) = M_{N_z} \end{aligned} \quad (4)$$

Using these cumulative products, the first derivative of the total transfer matrix in Eq. (3) can be written as:

$$\frac{dM}{dE} = \frac{dM_{N_z}}{dE}M^c_{\text{left}}(N_z-1) + \sum_{n=N_z-1}^{2} M^c_{\text{right}}(i+1)\frac{dM_i}{dE}M^c_{\text{left}}(i-1) + M^c_{\text{right}}(2)\frac{dM_1}{dE} \quad (5)$$

Therefore, we have reduced the problem of calculation of the first derivative of the total transfer matrix to calculation of the left and right arrays of cumulative products, and then using these arrays to calculate the sum of N_z parts in Eq. (3), each of which is a product of two or three elements, as in Eq. (5), thus requiring three loops. The total complexity of this algorithm is $\mathcal{O}(N_z)+\mathcal{O}(N_z)+\mathcal{O}(N_z) = 3\mathcal{O}(N_z) \sim \mathcal{O}(N_z)$, meaning that through the use of the arrays of cumulative products we have $\mathcal{O}(N_z)$ complexity for finding the first derivative of the total transfer matrix, which is the same complexity as for calculating the total transfer matrix in the standard TMM.

Note that Eq. (5) gives the first derivative of every element in the total transfer matrix $\frac{dm_{ij}}{dE}$. Since these are complex numbers, we are interested in the derivative of their modulus $\frac{d|m_{ij}|}{dE}$ which can be calculated as:

$$\frac{d|m_{ij}|}{dE} = \frac{d}{dE}\left(\sqrt{(\Re(m_{ij}))^2+(\Im(m_{ij}))^2}\right) = \frac{1}{|m_{ij}|}\left[\Re(m_{ij})\Re\left(\frac{dm_{ij}}{dE}\right)+\Im(m_{ij})\Im\left(\frac{dm_{ij}}{dE}\right)\right] \quad (6)$$

The dTMM approach consists of first sweeping the energy interval of interest in a coarse equidistant energy grid across which we calculate the derivative of matrix elements as in Eq. (6). We can then employ the incremental search algorithm to determine intervals where $\frac{d|m_{ij}|}{dE}$ changes sign, and finally invoke a zero-finding (i.e. bisection) algorithm in each interval. This allows us to calculate extrema of $\frac{d|m_{ij}|}{dE}$ and calculate the eigenvalues of the ODE under consideration. We note that the key difference between dTMM algorithm and standard TMM approach is that we do not need to repeat multiple iterations of adaptive mesh around each potential solution, but rather use a bisection (or any zero-finding) algorithm. In subsequent sections in this paper, we were able to achieve machine precision of eigenvalues in 30-40 iterations using the bisection algorithm, while to achieve the same precision with the adaptive mesh approach, we would need to apply a mesh of 1000 points several times.

Overall, the introduction of cumulative product arrays in Eq. (4) has allowed us to calculate the first derivative of the total transfer matrix in Eq. (3) with $\mathcal{O}(N_z)$ complexity. We note that this formalism can be extended towards calculation of higher derivatives of M. The dTMM approach therefore offers high precision at the lower numerical cost than the standard TMM approach, where the only additional requirement for its implementation is the analytical calculation of $\frac{dM_i}{dE}$ which depends on the ODE under consideration.

Note that our approach extends beyond eigenvalue problems, E in Eqs. (3)-(6) can represent any variable that affects the total transfer matrix, which will be illustrated by an example in Section 6.

3. Electron structure calculation via effective mass approximation

In this section, we develop a formal theoretical approach that applies Eqs. (1)-(6) on the Schrödinger equation under the effective mass approximation that is established in the literature as a standard approach of determining electron structure in quantum heterostructures.

We validate the dTMM approach by comparing with the solutions obtained by the FDM approach [38] for the case of parabolic and two-band nonparabolic subbands. We also offer an example of MQW structure for which the standard TMM method fails to accurately calculate the electronic structure. This example serves as the motivation for our development of the dTMM approach as we were able to achieve high precision solutions ~30 times faster than with a standard TMM approach.

3.1. Theoretical considerations

In nanostructures with one dimensional confinement of carriers, the Schrödinger equation under the effective mass approximation can be written as [35]:

$$-\frac{\hbar^2}{2}\frac{d}{dz}\frac{1}{m^*(z)}\frac{d\psi_n(z)}{dz} + U_{\text{eff}}(z)\psi_n(z) = E_n\psi_n(z) \quad (7)$$

where $m^*(z)$ is the electron effective mass along the growth direction which varies with position due to the changes in the material composition. $\psi_n(z)$ is the wavefunction (envelope function), E_n is the electron energy (at the subband minimum), and $U_{\text{eff}}(z)$ is the total effective potential energy $U_{\text{eff}}(z) = U_{\text{c}}(z) - eF_{\text{e}}z - e\varphi(z)$ which consists of the conduction band offset $U_{\text{c}}(z)$, the added bias potential energy due to the externally applied electric field F_{e} along the growth direction z and the electrostatic potential energy (Hartree term).

The TMM approach discretizes $U_{\text{eff}}(z)$ across an equidistant spatial grid of N_z segments as in Fig. 1. For each segment, Eq. (7) has a constant potential term and there is an analytical solution in the form $\psi(z_i) = A_i e^{k_i z_i} + B_i e^{-k_i z_i}$ where k_i is the wavevector $k_i^2 = \frac{2m_i^*(U_i-E)}{\hbar^2}$, which is a complex number. These analytical solutions need to satisfy two boundary conditions between each segment: the continuity of the wavefunction $\psi(z_i) = \psi(z_{i+1})$ and the continuity of probability current that yields the condition $\frac{1}{m_i^*}\frac{d\psi}{dz}|_{z_i} = \frac{1}{m_{i+1}^*}\frac{d\psi}{dz}|_{z_{i+1}}$. If we apply these boundary conditions and introduce substitutes $k_i = p$ and $k_{i+1} = q$, $q_{pq} = \frac{m_{i+1}^*}{m_i^*}\frac{p}{q}$, we can generate the transfer matrix at the i-th segment as [15]:

$$M_i = \frac{1}{2}\begin{bmatrix} (1+q_{pq})e^{(p-q)z_i} & (1-q_{pq})e^{-(p+q)z_i} \\ (1-q_{pq})e^{(p+q)z_i} & (1+q_{pq})e^{-(p-q)z_i} \end{bmatrix} \quad (8)$$

Equation (8) links analytical solutions on two adjacent segments on the spatial grid as $\begin{bmatrix} A_{i+1} \\ B_{i+1} \end{bmatrix} = M_i \begin{bmatrix} A_i \\ B_i \end{bmatrix}$. To obtain the transfer matrix of

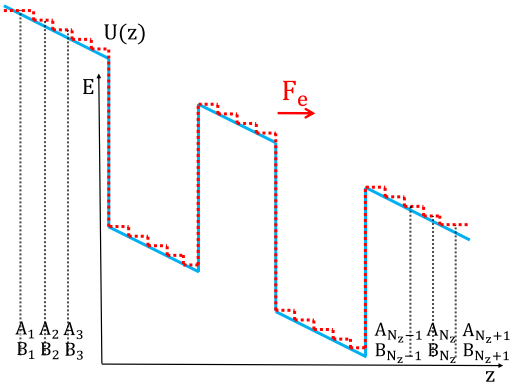

Fig. 1. Discretization of an exemplary effective potential energy profile $U_{\text{eff}}(z)$. The z-axis consists of N_z segments, for each segment there is a analytic solution allowing us to apply dTMM formalism.

the entire system, we need to repeat this process at each segment and link the first and the last point on the grid as:

$$\begin{bmatrix} A_{N_z+1} \\ B_{N_z+1} \end{bmatrix} = M \begin{bmatrix} A_1 \\ B_1 \end{bmatrix}$$
$$M = M_{N_z+1} M_{N_z} \ldots M_2 M_1 = \begin{bmatrix} m_{11} & m_{12} \\ m_{21} & m_{22} \end{bmatrix} \tag{9}$$

For quasi-bound electron states the coefficients A_{N_z+1} and B_1 have to be zero to avoid divergence of the wavefunctions. This imposes a condition $m_{11} = 0$ and the subsequent task in the standard TMM approach is to sweep potential eigenvalues for which this condition is satisfied. In practice, however, due to the finite size of the spatial grid, the $m_{11}(E)$ dependence does not tend to zero for each eigenvalue in identical manner. Additionally, m_{11} is a complex number. For some eigenvalues, $|m_{11}| \sim 10^{-16}$, but for some it may be $|m_{11}| \sim 10^{-3}$ and applying zero finding algorithms directly on $|m_{11}(E)|$ would not ensure uniform numerical precision of the eigenvalues. So we often need to seek minima of $|m_{11}(E)|$ instead.

The dTMM approach illustrated in Eqs. (4)-(6) requires us to calculate the first derivative of the transfer matrix in Eq. (8) whose elements are:

$$\begin{aligned}
\left.\frac{dM_i}{dE}\right|_{11} &= \frac{1}{2}\left[\frac{dq_{pq}}{dE} + (1+q_{pq})\left(\frac{dp}{dE} - \frac{dq}{dE}\right) z_i\right] e^{(p-q)z_i} \\
\left.\frac{dM_i}{dE}\right|_{12} &= \frac{1}{2}\left[-\frac{dq_{pq}}{dE} - (1-q_{pq})\left(\frac{dp}{dE} + \frac{dq}{dE}\right) z_i\right] e^{-(p+q)z_i} \\
\left.\frac{dM_i}{dE}\right|_{21} &= \frac{1}{2}\left[-\frac{dq_{pq}}{dE} + (1-q_{pq})\left(\frac{dp}{dE} + \frac{dq}{dE}\right) z_i\right] e^{(p+q)z_i} \\
\left.\frac{dM_i}{dE}\right|_{22} &= \frac{1}{2}\left[\frac{dq_{pq}}{dE} - (1+q_{pq})\left(\frac{dp}{dE} - \frac{dq}{dE}\right) z_i\right] e^{-(p-q)z_i}
\end{aligned} \tag{10}$$

where

$$\begin{aligned}
\frac{dq_{pq}}{dE} &= \frac{m^*_{i+1}}{m^*_i}\frac{\frac{dp}{dE}q - \frac{dq}{dE}p}{q^2} + \frac{p}{q}\frac{\frac{dm^*_{i+1}}{dE}m^*_i - \frac{dm^*_i}{dE}m^*_{i+1}}{m^{*2}_i} \\
\frac{dp}{dE} &= -\frac{m^*_i}{\hbar^2 p} + \frac{U_i - E}{\hbar^2 p}\frac{dm^*_i}{dE} \\
\frac{dq}{dE} &= -\frac{m^*_{i+1}}{\hbar^2 q} + \frac{U_{i+1} - E}{\hbar^2 q}\frac{dm^*_{i+1}}{dE}
\end{aligned} \tag{11}$$

In Eq. (11) we assumed that the effective mass $m^*(z)$ is dependent on eigenenergy E. This is a standard approach for consideration of nonparabolicity effects [35]. The most common approach for the effective mass dependence on energy is the two-band Kane approach $m^*_i = m_i\left(1 + \alpha_i(E - U_i)\right)$ where the nonparabolicity parameter α_i is taken as the reciprocal value of the bandgap energy. Thus the effective mass energy derivative would be $\alpha_i m_i$, where m_i is the bulk effective mass. The two-band Kane nonparabolic model can be simplified via the Taylor approximation [41] which results in the effective mass taking the form $m^*_i = m_i\left(1 - \alpha_i(E - U_i)\right)^{-1}$, thus the effective mass energy derivative is $m_i\alpha_i\left(1 - \alpha_i(E - U_i)\right)^{-2}$. This approximation is only valid for small values of the nonparabolicity parameter α_i. If nonparabolicity effect is neglected, all second terms in Eq. (11) are cancelled as the effective mass derivatives would be equal to zero.

Note that one of the advantages of both TMM and dTMM is that the nonparabolicity can be trivially treated in Eq. (11) via the energy dependent effective mass, which is not the case in FDM approaches [38] as Eq. (7) would need to be treated as a general eigenvalue problem.

3.2. Results and discussion

To validate the dTMM, we present the results of our numerical simulations for QCLs grown in different materials. We analyse three exemplary structures: Structure 1 is GaAs/AlGaAs bound to continuum (BTC) THz QCL designed for emission at 2 THz [42], Structure 2 is InGaAs/InAlAs longitudinal optical (LO) phonon THz QCL designed for high power operation [43], while Structure 3 is InGaAs/GaAsSb LO-phonon THz QCL designed for high performance over a spectral emission range between 3.3 and 4.0 THz [44]. Detailed description of the active medium of all three QCLs can be found in the Appendix.

The electron structure is calculated by numerical solving of Eq. (7) using the dTMM formalism presented in Eqs. (8)-(11) and we compare the results with the FDM approach [38,41]. We consider the parabolic subband approximation, the two-band Kane nonparabolicity model, as well as its Taylor approximation, which affect the terms in Eq. (11).

The results presented in Table 1 show the difference of subband energies between the dTMM and the FDM for the three exemplary structures.

In the dTMM approach we have used $dE = 0.1$ meV coarse step in order to detect sign changes of $\frac{d|m_{11}|}{dE}$ element and employed standard bisection method for zero finding with 10^{-16} eV tolerance that typically converged in 35-40 iterations around each eigenvalue. In Table 1 we can see that the dTMM and the FDM give very similar results that differ on the order of $10^{-5} - 10^{-7}$ eV. These results validate the dTMM numerically as the eigenvalues obtained by FDM inherently have machine precision.

The motivation for the development of the dTMM were the problems for which the standard TMM fails to accurately calculate the subband energies. One of the general drawbacks of TMM is that structures with large spatial length or structures with high barrier potentials that cause large mismatch in spatial profile of material parameters may cause the subband wavefunctions to diverge at the end of the spatial grid, indicating the lack of accuracy in the calculated eigenvalue. This problem could be resolved by several iterations of adaptive mesh algorithm, drastically increasing the numerical cost (CPU time). The dTMM on the other hand, is an ideal extension of the TMM as it offers higher precision at a lower numerical cost.

An example of a long-period structure with high potential barrier layers that is prone to this problem is the exemplary GaSb/AlSb THz structure designed for operation at 2.6 THz [45]. The detailed description of the active medium of this structure can be found in the Appendix as Structure 4.

Table 2 shows the comparison of the subband energies of the exemplary GaSb/AlSb structure calculated with the TMM and dTMM.

It shows that the subband energies of both methods are very similar, differing on the order of $10^{-6} - 10^{-5}$ eV. However, even at this magnitude the TMM approach generates diverging subband wavefunctions shown in Fig. 2. On the other hand, the calculated wavefunctions with the dTMM approach shown in Fig. 3 do not diverge, due to the higher accuracy of the calculated eigenvalues.

The efficiency of the dTMM approach is significantly better than the TMM approach. For a single subband energy, after we detect the mini-

Table 1
Absolute difference of subband energies between the new TMM and the FDM for all three different structures with resonant electrical bias values 1.9 kV/cm, 10 kV/cm and 8 kV/cm respectively. For each structure we show the results of the parabolic model, two band Kane nonparabolic model and its the two band Taylor approximation model in the first, second and third column respectively.

	Structure 1			Structure 2			Structure 3		
δE_1 [μeV]	0.74	1.23	1.22	9.27	0.34	0.94	0.54	1.96	0.83
δE_2 [μeV]	0.79	1.21	1.20	21.58	2.69	0.01	2.31	3.60	1.17
δE_3 [μeV]	0.69	1.05	1.04	26.95	1.95	1.00	2.25	5.75	2.77
δE_4 [μeV]	0.58	0.92	0.91	42.97	0.86	3.95	1.95	8.15	3.99
δE_5 [μeV]	0.39	0.91	0.90	...	...	...	...	...	...
δE_6 [μeV]	0.16	0.85	0.84	...	...	...	...	...	...
δE_7 [μeV]	0.13	0.67	0.66	...	...	...	...	...	...
δE_8 [μeV]	0.16	0.82	0.80	...	...	...	...	...	...
δE_9 [μeV]	2.31	2.67	2.66	...	...	...	...	...	...
δE_{10} [μeV]	2.61	3.12	3.13	...	...	...	...	...	...

Table 2
Energy of subband states in exemplary GaSb/AlSb THz structure for a resonant bias of 5.4 kV/cm calculated with the dTMM and TMM.

	TMM	dTMM
E_1 [meV]	25.40380	25.40546
E_2 [meV]	27.50423	27.50439
E_3 [meV]	60.35376	60.35366
E_4 [meV]	62.00911	62.00793
E_5 [meV]	64.99478	64.99611
E_6 [meV]	90.71985	90.71953
E_7 [meV]	115.64217	115.64195

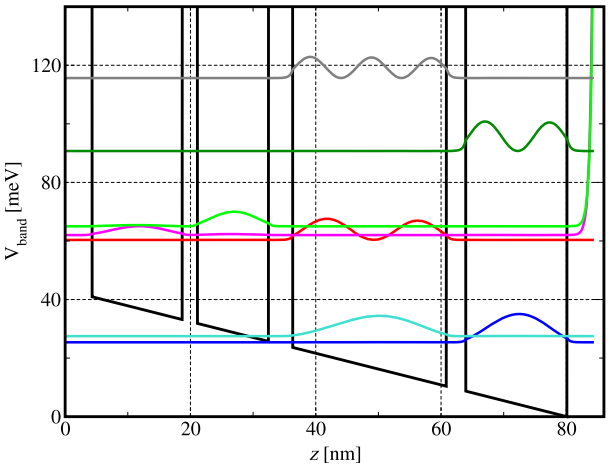

Fig. 2. Conduction band diagram of exemplary GaSb/AlSb THz structure [45] solved with standard TMM with diverging wavefunctions.

mum of m_{11} within interval dE, the standard TMM requires the adaptive mesh algorithm to apply the TMM again in i.e. 1000 points within the dE interval, thus having resolution of $dE/1000$, which is illustrated in the upper part of Fig. 4. On the other hand, the dTMM uses the incremental search algorithm to detect sign changes of $\frac{d|m_{11}|}{dE}$ and invokes the bisection algorithm across dE interval which rapidly converges by halving the energy interval. If for example $dE = 1$ meV, we need to apply 1000 points adaptive mesh four times for $10^{-12} \cdot dE$ eigenvalue accuracy and thus call $m_{11}(E)$ 4000 times achieving 10^{-15} eV precision, while the dTMM approach achieves $10^{-12} \cdot dE$ accuracy through ~ 37 ($2^{-37} = 7.3 \cdot 10^{-12}$) calls of $\frac{d|m_{11}|}{dE}$ calculation. Note that the dTMM has slightly higher memory storage requirements due to a need of storing cumulative product arrays in Eq. (4). Therefore, each call of $\frac{d|m_{11}|}{dE}$ has $3O(N_z)$ complexity, whereas each call of $m_{11}(E)$ has $O(N_z)$ complexity, meaning that the dTMM approach is $\sim 4000/3/37 \approx 36$ times faster than the standard TMM approach.

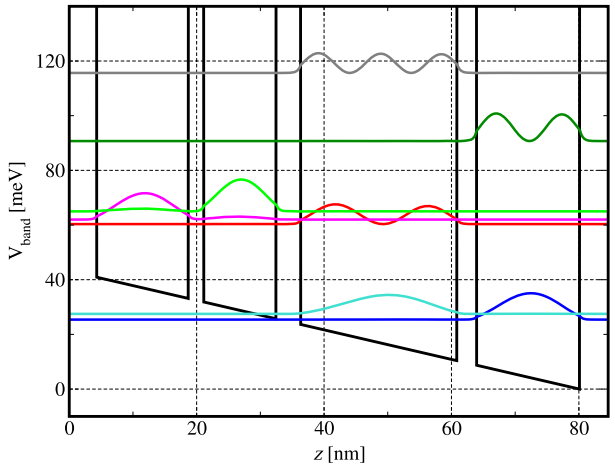

Fig. 3. Conduction band diagram of exemplary GaSb/AlSb THz structure [45] solved with the dTMM.

4. Electron structure calculation via 14 k·p nonparabolicity model

In the previous section the QCL electronic band structure is calculated using the single-band effective mass parabolic and two-band nonparabolic model. In earlier works [17,39] we have treated nonparabolicity via a more complex model that stems from 14 **k·p** band theory. The motivation for development of such models lies in growing interest in material systems where we want to manipulate the electron transport on several meV scale. Highly nonparabolic materials have a small bandgap and usually smaller electron effective mass which directly affects optical transitions. In this work, we apply the dTMM approach on the model used in [39] as this would serve modelling of electron transport in highly nonparabolic materials and also as an example how the dTMM approach handles 4$^{\text{th}}$ order ODE.

4.1. Theoretical considerations

In the two-band nonparabolic model the interaction of the conduction band and the light-hole valence band can be taken into account through the inclusion of energy-dependent electron effective mass in the 1D effective mass Schrödinger equation [35] in Eq. (7) and this can be treated as we presented in Eq. (11).

A more complex treatment of nonparabolicity was presented in [37] where the dispersion relation of the conduction band for a bulk III-V

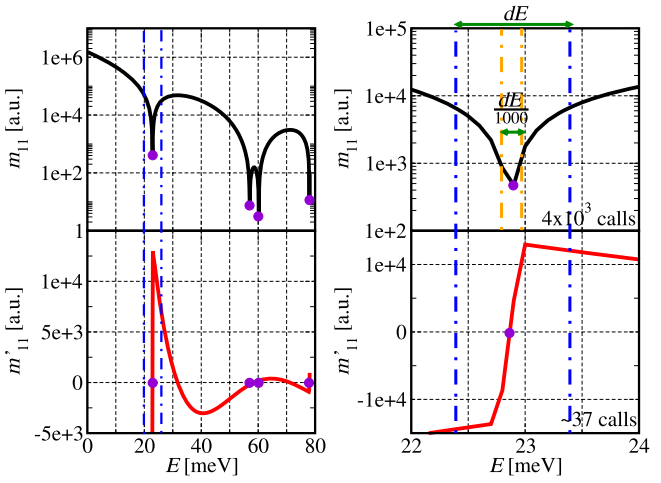

Fig. 4. Exemplary dependence of the m_{11} transfer matrix element and its first derivative $\frac{d|m_{11}|}{dE}$ versus energy (left). Minima of m_{11} ($\frac{d|m_{11}|}{dE}=0$) represent the eigenvalue solutions of the Schrödinger equation depicted by the purple circles for the exemplary electron structure of Structure 2 [43]. Plots on the right hand side illustrate the dependence of m_{11} and $\frac{d|m_{11}|}{dE}$ around one of the eigenvalues. The vertical dashed lines (blue) indicate the interval of energy dE in which we need to apply adaptive mesh algorithm for finding m_{11} minimum or $\frac{d|m_{11}|}{dE}$ zero finding incremental search algorithm in order to achieve machine precision of the eigenvalue solutions. Around one eigenvalue solution the adaptive mesh approach typically requires ~ 4000 calls of $m_{11}(E)$, while the zero finding incremental search algorithm (dTMM) can detect a zero within ~ 37 calls of $\frac{d|m_{11}(E)|}{dE}$. (For interpretation of the colours in the figure(s), the reader is referred to the web version of this article.)

material with a direct band gap was developed to the fourth order and the coefficients in the dispersion relation were calculated by solving the fourteenth order **k·p** model [46]. For nanostructures with one dimensional (1D) confinement this model results in the following form of the nonparabolic 1D effective mass Schrödinger equation:

$$\frac{d^2}{dz^2}\alpha^E(z)\frac{d^2\psi_n(z)}{dz^2}-\frac{\hbar^2}{2}\frac{d}{dz}\frac{1}{m(z)}\frac{d\psi_n(z)}{dz}+U_{\text{eff}}(z)\psi_n(z)=E_n\psi_n(z) \quad (12)$$

The effective mass in Eq. (12) is not energy dependent in this model. The nonparabolicity is treated through the parameter $\alpha^E(z)$ which is material dependent and quantifies the effect of nearby energy bands on the electron dispersion relation and should not be mistaken with the nonparabolicity parameter used in the two-band approximation, as $\alpha^E(z)$ in Eq. (12) has a complex dependence not only on the bandgap energy, but rather a plethora of band parameters as illustrated in [39]. In [39] we presented two approaches for calculating $\alpha^E(z)$. In this paper we will use formulas presented in [47] and use material band parameters from [48].

The TMM approach for Eq. (12) is similar to treatment of Eq. (7). Once the total potential $U_{\text{eff}}(z)$ is discretized on a spatial grid (Fig. 1), Eq. (12) folds into an analytically solvable biquadratic equation at each segment on the grid as $\alpha_i^E k_i^4+\frac{\hbar^2k_i^2}{2m_i}=E-U_i$ where only one branch of the solution is physical [17]. The wavefunction solution is $\psi(z_i)=A_ie^{k_iz_i}+B_ie^{-k_iz_i}$. The transfer matrix for Eq. (12) has to satisfy the two boundary conditions between adjacent segments on the grid: the continuity of the wavefunction $\psi(z_i)=\psi(z_{i+1})$ and the continuity of the probability current that yields the condition [17,39] $\left(2\alpha_i^Ek_i^2-\frac{\hbar^2}{2m_i}\right)\frac{d\psi}{dz}|_{z_i}=\left(2\alpha_{i+1}^Ek_{i+1}^2-\frac{\hbar^2}{2m_{i+1}}\right)\frac{d\psi}{dz}|_{z_{i+1}}$, and the transfer matrix for the i-th boundary on a spatial grid has the identical form as Eq. (8), where the difference is in the expressions for p,q,q_{pq}:

$$k_i^2=\frac{\hbar^2}{4|\alpha_i^E|m_i}\left[1-\sqrt{1-16|\alpha_i^E|(E-U_i)\left(\frac{m_i}{\hbar^2}\right)^2}\right]$$
$$p=k_i,\quad q=k_{i+1} \quad (13)$$
$$q_{pq}=\frac{2\alpha_i^Ep^2-\frac{\hbar^2}{2m_i}}{2\alpha_{i+1}^Eq^2-\frac{\hbar^2}{2m_{i+1}}}\frac{p}{q}$$

Note that the dispersion given with wavevector k_i in Eq. (13) is the only physical solution of biquadratic equations that results from Eq. (12) and this entire model is valid up to the energy $E_\pi=\frac{5}{9}E_{\max}$ where $E_{\max}=\frac{\hbar^4}{16|\alpha^E|(m)^2}$ at which the energy dispersion relation becomes concave (mathematically corresponding to a negative effective mass, which is nonphysical) [49].

The dTMM model yields the identical transfer matrix derivative as in Eq. (10), where the difference is in terms p,q,q_{pq} and their energy derivatives:

$$\frac{dq_{pq}}{dE}=\left[\frac{6\alpha_i^Ep^2-\frac{\hbar^2}{2m_i}}{2\alpha_{i+1}^Eq^3-\frac{\hbar^2}{2m_{i+1}}q}\frac{dp}{dE}-\frac{\left(2\alpha_i^Ep^3-\frac{\hbar^2}{2m_i}p\right)\left(6\alpha_{i+1}^Eq^2-\frac{\hbar^2}{2m_{i+1}}\right)}{\left(2\alpha_{i+1}^Eq^3-\frac{\hbar^2}{2m_{i+1}}q\right)^2}\frac{dq}{dE}\right] \quad (14)$$
$$\frac{dp}{dE}=\frac{m_i}{\hbar^2}\frac{1}{p+\frac{4|\alpha_i^E|m_i}{\hbar^2}p^3}$$
$$\frac{dq}{dE}=\frac{m_{i+1}}{\hbar^2}\frac{1}{q+\frac{4|\alpha_{i+1}^E|m_{i+1}}{\hbar^2}q^3}$$

The numerical implementation of the dTMM for Eq. (12) is therefore very similar to the treatment of Eq. (7). The key difference is in the wavevector expressions and their energy derivatives and the fact that the effective mass is not energy-dependent and nonparabolicity is treated within the expressions in the wavevectors in Eq. (13).

Note that the FDM for Eq. (12) is not cumbersome as treatment of Eq. (7) because effective mass does not depend on the energy, and Eq. (12) can be discretized with finite differences. However, doing so reveals some of the fundamental drawback of the FDM that were also discussed for Eq. (7) in [38]. Namely, the eigenvalues of matrix used for FDM approach may lead to spurious solutions that need to be manually removed. This process was handled automatically in [38], however, this is not possible for Eq. (12) as the FDM does not have a mechanism of ignoring the nonphysical dispersion branch that we have ignored in the TMM presented above. Applying the FDM approach on Eq. (12) therefore yields a set of correct solutions, spurious solutions and nonphysical solutions making it very challenging to select only the correct ones. For this reason, we will not discuss the FDM results of Eq. (12).

4.2. Results and discussion

We present the results of our numerical simulations for the QCLs presented in the previous section [42–44] grown in GaAs/AlGaAs, InGaAs/InAlAs, and InGaAs/GaAsSb respectively. The two-band Kane nonparabolic electron structure, as well as its Taylor approximation is calculated by numerical solving of Eq. (7) using the dTMM approach, while the 14 **k·p** nonparabolic electron structure is calculated by numerical solving of Eq. (12) also via the dTMM approach. The results are presented in Tables 3, 4 and 5.

The results in Tables 3, 4 and 5 show that the nonparabolicity increases the energy of the subbands and affects higher subbands more than lower ones. We can see that the 14 **k·p** nonparabolic model in general produces a stronger effect than the two-band nonparabolic model,

Table 3
Energy of subband states in the exemplary GaAs/AlGaAs BTC THz QCL [42] for a resonant bias of 1.9 kV/cm shown for the parabolic model, two-band Kane nonparabolic model, as well as its Taylor approximation and the 14 **k**·**p** nonparabolic model.

	Parabolic	Kane	Taylor	14 **k**·**p**
E_1 [meV]	17.7071	17.7780	17.7708	18.3292
E_2 [meV]	20.6693	20.7204	20.7147	21.2403
E_3 [meV]	22.9848	23.0249	23.0200	23.4719
E_4 [meV]	25.1394	25.1735	25.1689	25.5640
E_5 [meV]	26.9686	27.0236	27.0157	27.4512
E_6 [meV]	29.9409	29.9913	29.9814	30.4052
E_7 [meV]	32.7406	32.7618	32.7549	33.0735
E_8 [meV]	41.8661	41.7628	41.7526	42.0859
E_9 [meV]	58.4094	57.6049	57.5769	58.0818
E_{10} [meV]	62.1036	61.0577	61.0129	61.6258

Table 4
Energy of subband states in the exemplary InGaAs/InAlAs LO-phonon THz QCL [43] for a resonant bias of 10 kV/cm shown for the parabolic model, two-band Kane nonparabolic model, as well as its Taylor approximation and the 14 **k**·**p** nonparabolic model.

	Parabolic	Kane	Taylor	14 **k**·**p**
E_1 [meV]	22.8640	23.2619	23.1124	23.5196
E_2 [meV]	57.0385	56.8035	56.4867	58.1573
E_3 [meV]	60.1812	60.4932	60.0862	61.7031
E_4 [meV]	77.9856	78.6086	78.1281	79.5514

Table 5
Energy of subband states in the exemplary InGaAs/GaAsSb LO-phonon THz QCL [44] for a resonant bias of 8 kV/cm shown for the parabolic model, two-band Kane nonparabolic model, as well as its Taylor approximation and the 14 **k**·**p** nonparabolic model.

	Parabolic	Kane	Taylor	14 **k**·**p**
E_1 [meV]	20.7661	21.0584	20.9500	21.2180
E_2 [meV]	51.4799	51.5901	51.4372	53.8374
E_3 [meV]	56.0809	55.6355	55.2439	56.0760
E_4 [meV]	70.2315	70.5727	70.2359	71.2781

which is expected as it is a result of the fourteenth order **k**·**p** model and takes into account the interaction of the lowest conduction band with the light-hole and heavy-hole valence band, split-off band and three higher conduction bands, whereas the two-band model takes into account only the interaction of the conduction band and the light-hole valence band.

We can also observe that, in general, the nonparabolic effects are greater in InGaAs/InAlAs and InGaAs/GaAsSb structures than in GaAs/AlGaAs structures, which is expected as these elements have smaller bandgaps and thus a higher nonparabolicity parameter [39].

The two band nonparabolic Taylor approximation model gives similar results compared to the two-band Kane nonparabolic model for the GaAs/AlGaAs structures, but is less accurate in InGaAs/InAlAs and InGaAs/GaAsSb structures because of their higher nonparabolicity parameter, which make the Taylor approximation less valid.

5. Numerical performance

In previous sections we validated the dTMM approach by analysing various structures. The overall complexity of this method for calculating eigenvalues is $O(N_i \log_2(\frac{dE}{\epsilon})N_z)$. The eigenvalue grid of N_i intervals is first traversed linearly in order to identify the intervals containing the zeroes of the function, followed by a bisection algorithm in these intervals, where dE is the length of each interval and ϵ is the desired precision, and each call of the $\frac{d|m_{11}|}{dE}$ function has linear complexity $O(N_z)$ for traversing the spatial grid. Typically the number of intervals in which the bisection algorithm is called is significantly lower than N_i and in most cases of interest is less than 20. On the other hand, the FDM approaches have $O(N_z^3)$ complexity [50], thus it may not be immediately clear how well these methods compare. FDM solvers require storage of square matrices, while dTMM traverses the spatial grid linearly thus should be faster because we need to store three arrays of N_z size instead. This means that spatial complexity of the dTMM model is lower than the space complexity of the FDM approach and this will affect the time complexity as well. This work is accompanied by seven different numerical solvers written in MATLAB. For analysis in this paper we used C++ for their implementation due to superior performance. To benchmark our solvers, we chose the BTC structure analysed in Section 3 (structure 1) due to its rich electronic structure (10 eigenvalues of interest and 1276 Å period length as illustrated in the Appendix).

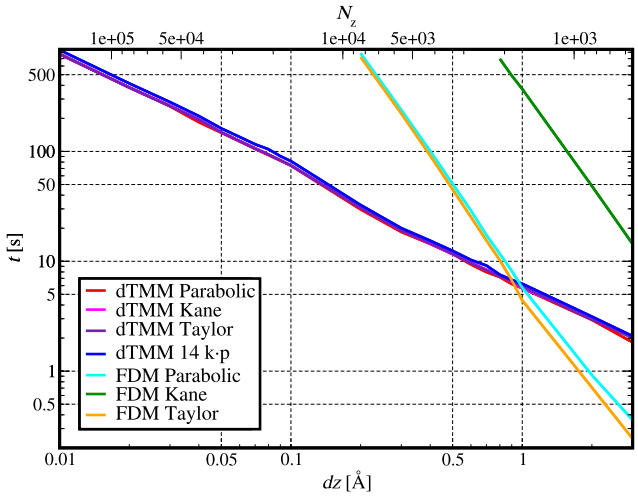

Fig. 5. Time performance of numerical solvers in this work versus spatial step size (bottom x-axis) and spatial resolution (top x-axis) of the numerical grid applied to BTC THz QCL [42]. The FDM solvers were unable to handle higher spatial resolution due to matrix storage requirements.

The time performance of our solvers is presented in Fig. 5. Numerical analysis in this work was undertaken on Intel Xeon Gold 6138 CPUs. The FDM Kane solver employs full nonparabolicity models as in [38] that requires solving a general fourth order polynomial eigenvalue problem. This solver has higher spatial complexity as it requires storage of $4N_z \times 4N_z$ matrix of FDM coefficients making it the slowest. The Taylor approximation of Kane nonaprabolicity and parabolic solver require $N_z \times N_z$ matrix thus their time performance is faster and comparable. The TMM solvers, regardless of the nonparabolicity type do not require matrices and typically only need to linearly transverse the spatial grid. For this reason, the TMM solvers have comparable performance and are able to handle much higher spatial resolution than FDM solvers due to their lower spatial complexity. The FDM solvers only outperform the dTMM method for low spatial resolution.

In Fig. 6 we showcase the convergence test of calculated eigenvalues as spatial resolution is varied. Interestingly, all models follow similar trends. We can observe that solutions are converging with smaller spatial step size, but the FDM models were unable to handle very high resolution. A very interesting result is that although the FDM solutions have inherent machine precision, the eigenvalues calculated for two different step sizes may differ even on a scale of 10^{-2} meV. We attribute this to the bandstructure potential profile and numerical peculiarities that follow it, we note that our potential profile has step-like variation at interfaces between two materials, and these cause delta-like variations when derivatives in Eq. (7) are calculated. This does not cause the FDM method to diverge, but numerically may impact the convergence. Overall, the spatial resolution introduces and error in all solvers thus

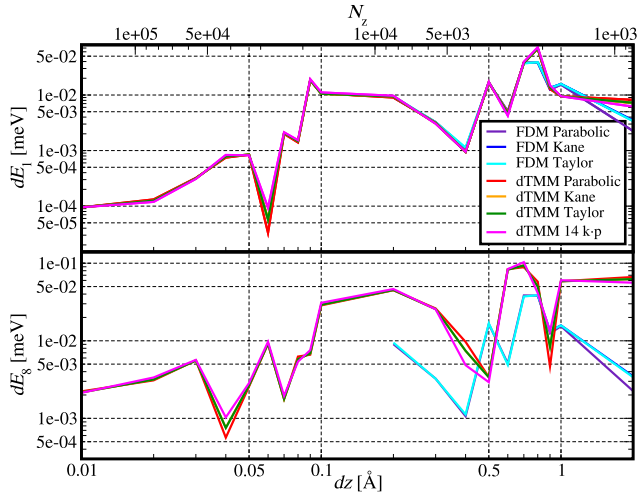

Fig. 6. Convergence of calculated ground and lasing level states versus spatial step size (bottom x-axis) and spatial resolution (top x-axis) for BTC THz QCL [42]. The convergence is calculated as energy difference between consecutive solutions as spatial resolution is varied. The range of spatial step size was an array between 0.01 and 2 Å.

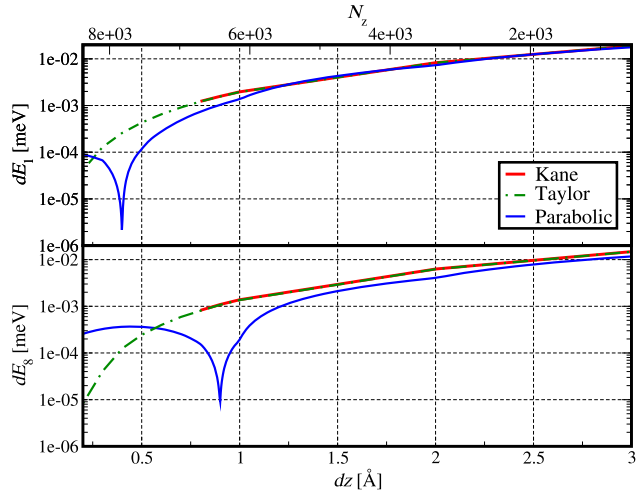

Fig. 7. Energy difference between complementary FDM and TMM solvers versus spatial step size (bottom x-axis) and spatial resolution (top x-axis) for BTC THz QCL [42].

affecting the convergence of the solvers as it is varied. In Table 1 we present the energy differences between complementary TMM and FDM models for various structures for a fixed spatial resolution. In Fig. 7 we focus on Structure 1 from Section 3 and present the difference between the complementary TMM and FDM models (i.e. |TMM Kane - FDM Kane| etc.) as spatial resolution is varied. This comparison is limited as FDM approaches are unable to handle higher resolutions, but we can observe that the solutions are more comparable as spatial step size is reduced. The mismatch between the two solvers can be attributed to convergence issues we observed in Fig. 6. While all our solvers have very high precision of the corresponding eigenvalues, these solutions are not necessarily comparable as these methods have different error dependence on spatial step size.

6. Interface optical phonons

One of the key electron scattering mechanisms in semiconductor structures is the interaction between electrons and optical phonons. The scattering models typically use bulk phonons even in heterostructures and devices based on superlattices. While this is a good approximation, a more physically correct model should take into account the effect of confinement on the optical-phonon modes resulting in interface (IF) phonon modes and confined (CF) phonon modes.

6.1. Theoretical considerations

Interface modes are localized at the interfaces of the heterostrucure, while confined modes can be regarded as bulk modes that are segmented by the hetorstructure interfaces. These phonon modes are calculated within the macroscopic dielectric continuum model [51,52] which is based on the production of an electric polarisation $P(r)$ due to the lattice vibrations. The DCM describes the phonon modes through their electrostatic potential along the heterostructure. For a medium of dielectric constant $\epsilon(\omega)$ these equations are given by:

$$\begin{aligned} &\nabla \cdot \boldsymbol{D}(\boldsymbol{r}) = \rho_0(\boldsymbol{r}) \\ &\boldsymbol{D}(\boldsymbol{r}) = \epsilon \boldsymbol{E}(\boldsymbol{r}) = \epsilon_0 \boldsymbol{E}(\boldsymbol{r}) + \boldsymbol{P}(\boldsymbol{r}) \\ &\boldsymbol{E}(\boldsymbol{r}) = -\nabla \phi(\boldsymbol{r}) \end{aligned} \tag{15}$$

where $\boldsymbol{D}(\boldsymbol{r})$, $\boldsymbol{E}(\boldsymbol{r})$, $\boldsymbol{P}(\boldsymbol{r})$ and $\phi(\boldsymbol{r})$ are the electric displacement, electric field, electric polarization and electrostatic scalar potential. $\rho_0(\boldsymbol{r})$ is the free charge density, and ϵ and ϵ_0 are the dielectric permittivity of the respective material and of free space. Using the generalized Lyddane–Sachs–Teller relation, $\epsilon(\omega)$ can be written as a single pole function:

$$\epsilon(\omega) = \epsilon_\infty \frac{\omega^2 - \omega_{\mathrm{LO}}^2}{\omega^2 - \omega_{\mathrm{TO}}^2} \tag{16}$$

for a binary alloy, and a double pole function:

$$\epsilon(\omega) = \epsilon_\infty \frac{(\omega^2 - \omega_{\mathrm{LO1}}^2)(\omega^2 - \omega_{\mathrm{LO2}}^2)}{(\omega^2 - \omega_{\mathrm{TO1}}^2)(\omega^2 - \omega_{\mathrm{TO2}}^2)} \tag{17}$$

for a ternary alloy [53], where ϵ_∞ is the high frequency dielectric constant of the alloy. LO and TO stand for the longitudinal and transverse optical mode, and 1 and 2 denote the respective material.

In the case of free oscillation $\rho_0(\boldsymbol{r}) = 0$ and Eq. (15) lead to the condition $\epsilon(\omega)\nabla^2\phi(\boldsymbol{r}) = 0$. In bulk materials this equation leads to the bulk optical phonons that satisfy the nontrivial condition $\epsilon(\omega) = 0$. For quantum well systems that are confined along the crystal growth direction z and have no constraint in the $x-y$ plane the electrostatic potential $\phi_i(\boldsymbol{r})$ and its Fourier transform $\phi_i(q, z)$ in the region $[z_{i-1}, z_i]$ can be written as $\phi_i(\boldsymbol{r}) = \sum_q e^{-i\boldsymbol{q}\cdot\boldsymbol{\rho}}\phi_i(q, z)$ where $\boldsymbol{\rho}$ and $\boldsymbol{q}$ are the position and wave vector in the $x-y$ plane of the interface. This yields the following ODE:

$$\epsilon(\omega)\left(\frac{\partial^2}{\partial z^2} - q^2\right)\phi_i(q, z) = 0 \tag{18}$$

The solutions of Eq. (18) satisfy either $\epsilon(\omega) = 0$ which yields CF (bulk) phonon modes or $\left(\frac{\partial^2}{\partial z^2} - q^2\right)\phi_i(q, z) = 0$ which correspond to IF optical phonon modes.

The CF modes resulting from Eq. (18) due to the condition $\epsilon(\omega) = 0$ are $\omega = \omega_{\mathrm{LO}}$ for binary alloys and $\omega = \omega_{\mathrm{LO}}$ or $\omega = \omega_{\mathrm{TO}}$ for ternary alloys. These modes are bulk-like and propagate in a single layer between two interfaces from which they are fully backscattered because the neighbouring layers have different optical phonon frequencies. The electrostatic potentials of the CF modes form an orthogonal and complete set and one of the possible sets of electrostatic potentials that satisfy the conditions of confined phonon modes is [54,55]:

$$\phi_i^{\mathrm{CF}}(q, z_i) = \left(\frac{\hbar}{\epsilon_0}\frac{1}{d\epsilon_i(\omega)/d\omega}\right)^{1/2}\left(\frac{1}{q^2 + (m\pi/a_i)^2}\right)^{1/2} \left(\frac{2}{a_i}\right)^{1/2} \sin\frac{m\pi}{a_i}(z - z_i) \tag{19}$$

in which $m = 1, 2, 3...$, $z_i < z < z_i + a_i$, where a_i represents the width of different layers.

Unlike the CF modes whose electrostatic potentials can be analytically found in Eq. (19), the electrostatic potentials of the IF modes can only be calculated numerically. To numerically calculate the IF modes in Eq. (18) we can apply the TMM/dTMM approach as Eq. (18) has straightforward solutions on each segment once the spatial axis is discretized $\phi_i(q,z) = A_i e^{qz} + B_i e^{-qz}$.

All modes in Eq. (18) need to satisfy the boundary conditions of the DCM approach which require that the tangential component of the electric field and the normal component of the electrical displacement are continuous [52,56–58] at each interface yielding $\phi_i(q,z_i) = \phi_{i+1}(q,z_i)$ and $\epsilon_i \frac{\partial}{\partial z}\phi_i(q,z_i) = \epsilon_{i+1}\frac{\partial}{\partial z}\phi_{i+1}(q,z_i)$. The transfer matrix of the i-th segment then reads:

$$M_i = \frac{1}{2}\begin{bmatrix} (1+\epsilon_i/\epsilon_{i+1}) & (1-\epsilon_i/\epsilon_{i+1})e^{-2qz_i} \\ (1-\epsilon_i/\epsilon_{i+1})e^{2qz_i} & (1+\epsilon_i/\epsilon_{i+1}) \end{bmatrix} \tag{20}$$

The TMM approach can link segmented matrices in Eq. (20) to obtain the dispersion relation and electrostatic potential of IF phonons [40] due to the fact that similarly to the case of the electron structure and the subband state wavefunctions coefficients A_{N_z} and B_1 need to be zero so that the solutions of the electrostatic phonon potential do not diverge as z approaches $\pm\infty$. This leads to the same condition $m_{11} = 0$ for the IF phonon modes as for the electron structure in Eq. (9). The difference is that we are not seeking eigenvalues of Eq. (18), but rather frequency modes ω that satisfy the $m_{11} = 0$ condition. Therefore, the process requires manual sweep of ω similarly to how energy was swept for the Schrödinger equation in previous sections. We can also convert angular frequency sweep to energy sweep using relation $E = \hbar\omega$ where E would represent energy of phonon modes that correspond to interface modes.

We can extend TMM by applying dTMM formalism as we have established its numerical superiority over standard TMM. We need to seek the energy derivative of Eq. (20):

$$\frac{dM_i}{dE} = \frac{1}{2}\begin{bmatrix} \frac{dt_i}{dE} & -\frac{dt_i}{dE}e^{-2qz_i} \\ -\frac{dt_i}{dE}e^{2qz_i} & \frac{dt_i}{dE} \end{bmatrix} \tag{21}$$

where we have introduced substitute $t_i = \epsilon_i/\epsilon_{i+1}$ and it applies:

$$\begin{aligned} \frac{dt_i}{dE} &= \frac{1}{\hbar}\frac{dt_i}{d\omega} = \frac{1}{\hbar}\frac{\frac{d\epsilon_i}{d\omega}\epsilon_{i+1} - \frac{d\epsilon_{i+1}}{d\omega}\epsilon_i}{\epsilon_{i+1}^2} \\ \frac{d\epsilon_i^{\text{binary}}}{d\omega} &= \epsilon_{\infty i}\frac{2\omega(\omega_{\text{LO}}^2 - \omega_{\text{TO}}^2)}{(\omega^2 - \omega_{\text{TO}}^2)^2} \\ \frac{d\epsilon_i^{\text{ternary}}}{d\omega} &= 2\omega\epsilon_{\infty i}\left[\frac{(\omega_{\text{LO1}}^2 - \omega_{\text{TO1}}^2)}{(\omega^2 - \omega_{\text{TO1}}^2)^2}\frac{(\omega^2 - \omega_{\text{LO2}}^2)}{(\omega^2 - \omega_{\text{TO2}}^2)}\right. \\ &\quad \left. + \frac{(\omega_{\text{LO2}}^2 - \omega_{\text{TO2}}^2)}{(\omega^2 - \omega_{\text{TO2}}^2)^2}\frac{(\omega^2 - \omega_{\text{LO1}}^2)}{(\omega^2 - \omega_{\text{TO1}}^2)}\right] \end{aligned} \tag{22}$$

where we need to adjust the permittivity derivatives as they differ for binary and ternary material system heterostructures.

The values of the high frequency dielectric constants and the phonon energies for GaAs/$Al_xGa_{1-x}As$ systems are given in Table 6 [59].

Using equations (20) and (21) we can implement the dTMM method as discussed in Section 2 and minimize $|m_{11}|$ using Eq. (6). Once the IF phonon mode energies are found, determination of the electrostatic potential of each mode is reduced to matrix multiplication for calculating the coefficients A_i and B_i for each layer.

We note that in a MQW system with n interfaces in the case of an all-binary heterostructure (for example GaAs/AlAs system) there are $2n$ IF phonon modes, whereas for a structure with alternating binary and ternary layers (for example GaAs/$Al_xGa_{1-x}As$ system), there are $3n$ IF phonon modes, due to the fact that each ternary layer has two binary-like modes [40].

Table 6
High frequency dielectric constants and phonon energies [59] used in the calculation of the dispersion relations.

	GaAs	AlAs	$Al_xGa_{1-x}As$
ϵ_∞	10.89	8.16	10.89-2.73x
$\hbar\omega_{\text{LO1}}$ [meV]	36.25	...	36.25-6.55x+1.79x^2
$\hbar\omega_{\text{TO1}}$ [meV]	33.29	...	33.29-0.64x-1.16x^2
$\hbar\omega_{\text{LO2}}$ [meV]	...	50.09	44.63+8.78x-3.32x^2
$\hbar\omega_{\text{TO2}}$ [meV]	...	44.88	44.63+0.55x-0.30x^2

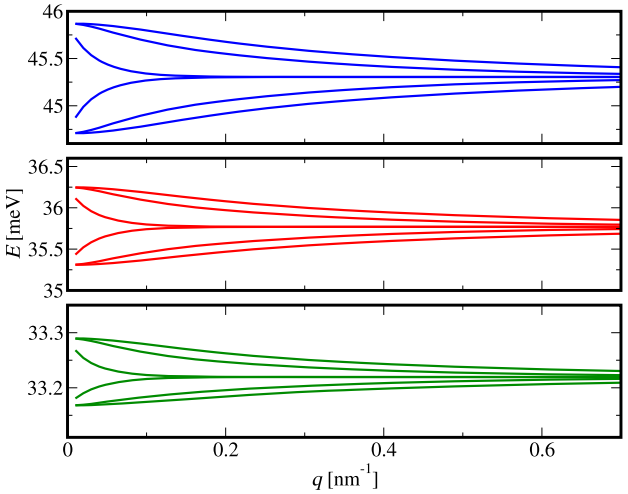

Fig. 8. IF phonon dispersion relations of each group of IF phonon modes shown for the exemplary THz QCL [61] with a GaAs/$Al_{0.15}Ga_{0.85}As$ material combination.

After finding the electrostatic potential of each IF phonon mode we need to apply the energy normalization condition [40,60]:

$$\frac{\hbar}{2\omega} = \sum_k \frac{\epsilon_0}{2\omega}\frac{d\epsilon_k(\omega)}{d\omega}\int_{R_k}\left(q^2|\phi_i(q,z)|^2 + \left|\frac{\partial\phi_k(q,z)}{\partial z}\right|^2\right)dz \tag{23}$$

where the summation goes over all the layers of the structure and R_k represents intervals $R_k = [z_i, z_{i+1}]$.

6.2. Results and discussion

In this section we apply the dTMM approach for calculating the interface phonon dispersion relations and electrostatic phonon potentials of an exemplary LO-phonon design THz QCL that achieved pulsed operation at a high temperature of 200 K [61], whose detailed description of the active medium can be found in the Appendix as Structure 5.

The dTMM approach for IF modes allows us to find the dispersion relations and the energy of the interface phonon modes for different values of phonon wave vector q, ranging in $q \in [0,1]$ nm^{-1}. The dispersion relations are shown in Fig. 8.

In Fig. 8 we can observe that the IF optical phonon modes form three groups, each of which consists of 6 modes, resulting in a total of 18 modes. As the exemplary QCL has 6 binary material/ternary material (GaAs/$Al_{0.15}Ga_{0.85}As$) interfaces, the expected number of IF modes is $3 \cdot 6 = 18$. The ternary barrier layers have both GaAs-like and AlAs-like modes, and the GaAs-like modes in $Al_{0.15}Ga_{0.85}As$ differ from the ones in GaAs layers, which results in a double number of both LO and TO GaAs phonon modes. The formed IF modes are joint modes of the similar GaAs and GaAs-like modes of the different material layers [40].

The lowest group of modes is located between the GaAs TO mode energy of 33.29 meV in GaAs layers, and the GaAs-like TO mode energy

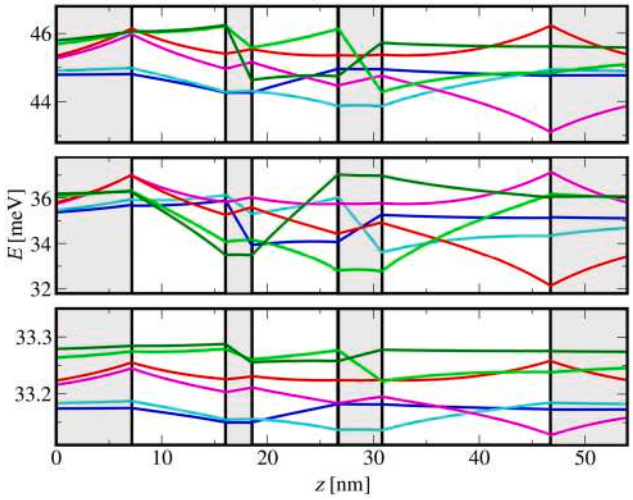

Fig. 9. Electrostatic potential of the 18 IF optical modes for a wave vector q = 0.1 nm^{-1} shown for the exemplary THz QCL [61]. The $Al_{0.15}Ga_{0.85}As$ barrier layers are shaded.

of 33.168 meV in $Al_{0.15}Ga_{0.85}As$ layer. Due to the fact that the energy difference between these two is very small, this group of modes shows very little dispersion, which can be seen in Fig. 8. The middle group of modes is located between the GaAs LO mode energy of 36.25 meV in GaAs layers, and the GaAs-like LO mode energy of 35.308 meV in $Al_{0.15}Ga_{0.85}As$ layer and has significantly larger dispersion compared to the TO group of modes. The third group of modes is located between the AlAs-like LO mode energy of 45.872 meV, and the AlAs-like TO mode energy of 44.706 meV in $Al_{0.15}Ga_{0.85}As$ layers. This group has the largest dispersion of the three groups.

Once the dispersion relations are found, the electrostatic potential of each mode for each wave vector is found using the TMM and normalised so that it satisfies the energy normalization condition (23). The electrostatic potential of the 18 IF optical modes are shown in Fig. 9 for a wave vector q = 0.1 nm^{-1}.

In Fig. 9 we can see that the electrostatic potentials are linear combinations of exponentially growing and exponentially damped spatial functions. We note that all calculated IF modes in Fig. 8 are in the vicinity of the bulk-like CF modes which justifies neglecting the IF modes in electron transport models [62]. This agrees well with the literature [63] which reports that inclusion of CF and IF phonon modes in a GaAs/AlGaAs QCL increases the electron-LO phonon scattering rates negligibly and induces minor corrections to the electron transport when compared to the results obtained in the bulk phonon approximation.

7. Conclusion

The TMM approach has a long history of application due to its intuitive and semi-analytical nature, but it is often criticized as numerically inefficient in comparison to the FDM approaches. The key benefit of the TMM approach over the FDM is its lower spatial complexity, allowing for higher spatial resolution, however the main criticism when the TMM is used for eigenvalue problems is its numerical cost when attempting to achieve machine precision. Our work exploits the semi-analytical nature of the TMM approach and extends it to the dTMM which is capable of matching the numerical precision and efficiency of the FDM approaches.

In Section 2 we have introduced a general mathematical formalism that can be used for a wide range of problems that deal with ordinary differential equations and eigenvalue problems, which allows the dTMM approach to exhibit high numerical precision at a lower computational cost than the standard TMM approach. This has been achieved due to the fact that the standard TMM consists in finding the minimum of the modulus $|m_{ij}|$ of the element of the total transfer matrix $M(E)$ by seeking solutions in shooting-like manner, often requiring adaptive mesh algorithms to boost precision. The dTMM utilizes the analytically calculated first derivative of $\frac{d|m_{ij}|}{dE}$, allowing the use of a plethora of numerically efficient zero-finding algorithms that can achieve machine precision.

The calculation of the electronic structure of multiple quantum well heterostructures, such as QCL, from the numerical accuracy point of view is a very demanding. The challenge lies in the requirement of high eigenvalue precision and high spatial resolution which cannot be handled efficiently by the FDM approaches due to the large matrix size. Our analysis has shown that the dTMM approach is both as precise and can handle higher spatial resolution than the FDM models:

- We analysed the 1D effective mass Schrödinger equation in Section 3 treating parabolic, two-band Kane nonparabolic as well as its Taylor approximation.
- We validated the model by analysing electronic structure of QCLs grown in different material combinations by comparing the dTMM approach with the FDM approach [38].
- We illustrated the importance of numerical precision by providing an example of a structure that yields diverging solutions due to inaccuracy of the TMM approach, and how this can be resolved by the dTMM at higher numerical efficiency.
- We demonstrated how the dTMM can be applied to a more complex ODE in Section 4 by analyzing a 4th order Schrödinger equation that results from 14 **k·p** treatment and takes into account the interaction of the lowest conduction band with the light-hole and heavy-hole valence band, split-off band and three higher conduction bands.
- We have compared the numerical performance of the dTMM and the FDM in Section 5. The FDM solvers were unable to handle higher spatial resolution due to matrix storage requirements while the dTMM solvers were able to handle much higher spatial resolution due to their lower spatial complexity and outperform the FDM solvers in terms of time performance.

As an example of the versatility of the dTMM approach, in Section 6 we analysed interface optical phonon dispersion in semiconductor heterostructers. The electron-longitudinal phonon interaction is one of the key transport mechanisms in QCLs, often approximated by bulk treatment only, and not taking into account the effect of layer variation in the heterostructure. Our work provides a more realistic optical phonon treatment where bulk phonons are replaced with confined and interface phonons. We have shown how the dTMM approach can be used for calculation of the IF phonon modes dispersion relations and the electrostatic potential of each mode within the dielectric continuum model.

The analysis we conducted in this paper is accompanied by the corresponding numerical package, released in MATLAB version that can be found on https://github.com/AcaDemicNanoLab/dTMM_Schrodinger.

Overall, we have introduced a novel method that has resolved several shortcomings of the transfer matrix method, and our formalism can be further generalised and extended to a verity of problems. The key advantage of our dTMM approach is that it keeps the intuitive and semi-analytical nature of the TMM while having high numerical precision, lower computational cost and can outperform FDM methods when handling high spatial resolution.

CRediT authorship contribution statement

N. Stanojević: Writing – original draft, Visualization, Software, Methodology, Investigation, Data curation, Conceptualization. **A. Demić:** Writing – review & editing, Visualization, Software, Methodology, Investigation, Data curation, Conceptualization. **N. Vuković:** Writing – review & editing, Funding acquisition, Conceptualization. **P. Dean:** Supervision, Funding acquisition. **Z. Ikonić:** Conceptualization. **D. Indjin:** Supervision, Funding acquisition, Conceptualization. **J. Radovanović:** Supervision, Funding acquisition, Conceptualization.

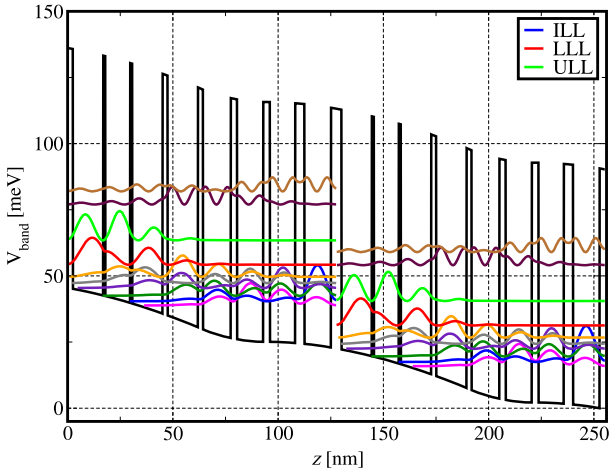

Fig. 10. Conduction band potential of the exemplary GaAs/AlGaAs BTC THz QCL along with moduli squared of the corresponding wavefunctions [42]. The layer thicknesses, starting with the injection barrier are **5.0**/14.4/**1.0**/11.8/**1.0**/14.4/**2.4**/14.4/**2.4**/13.2/**3.0**/12.4/**3.2**/12.0/**4.4**/12.6 nm, where $Al_{0.1}Ga_{0.9}As$ barriers are shown in bold, and wells doped to $1.3 \cdot 10^{16}$ cm^{-3} are underlined.

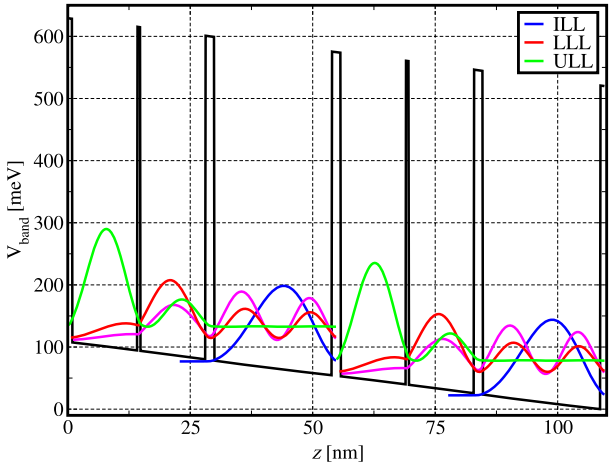

Fig. 11. Bottom of the conduction band potential of the exemplary InGaAs/InAlAs LO-phonon THz QCL along with moduli squared of the corresponding wavefunctions [43]. The layer thicknesses, starting with the injection barrier are **1.8**/13.3/**0.6**/13.3/**1.8**/(9.0+6.0+9.0) nm. The well layers are made of $In_{0.53}Ga_{0.47}As$ and the $In_{0.52}Al_{0.48}As$ barriers are shown in bold. The middle part of the well doped to $3.3 \cdot 10^{16}$ cm^{-3} is underlined.

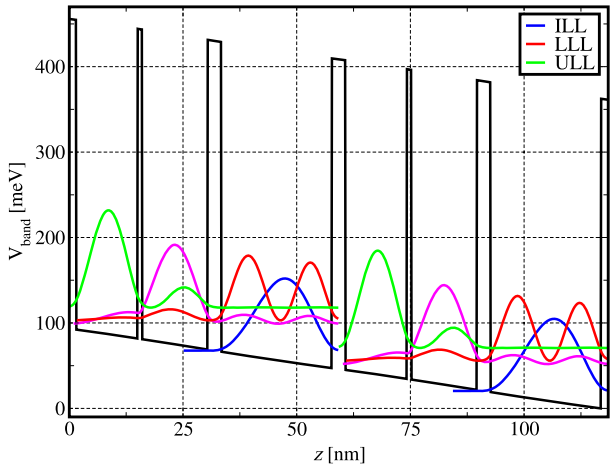

Fig. 12. Bottom of the conduction band potential of the exemplary InGaAs/GaAsSb LO-phonon THz QCL along with moduli squared of the corresponding wavefunctions [44]. The layer thicknesses, starting with the injection barrier are **3.0**/13.5/**1.0**/14.4/**3.0**/2.0/20.3/2.0 nm. The well layers are made of $In_{0.53}Ga_{0.47}As$ and the $GaAs_{0.51}Sb_{0.49}$ barriers are shown in bold. The well doped to $1.0 \cdot 10^{16}$ cm^{-3} is underlined.

Declaration of competing interest

The authors declare that they have no known competing financial interests or personal relationships that could have appeared to influence the work reported in this paper.

Acknowledgements

This work was financially supported by the Vlatacom Institute of High Technologies under project 178, the Ministry of Science, Technological Development and Innovation of the Republic of Serbia under contract number: 451-03-65/2024-03/200103, “DEMETRA: Development of high-performance mid-IR / THz quantum cascade lasers for advanced applications”, Science Fund of the Republic of Serbia, Serbian Science and Diaspora Collaboration Programme: Knowledge Exchange Vouchers, Grant Number 6436915, Science Fund of the Republic of Serbia, Grant No. 10504, “Ultra-short pulsations from TERAhertz quantum cascade laser using passive mode-LOCKing with graphene saturable absorber” - TERALOCK, European Cooperation in Science and Technology (COST) Action CA21159 PhoBioS, the Engineering and Physical Sciences Research Council (EPSRC) UK (Grants No. EP/W028921/1, No. EP/T034246/1, and No. EP/V004743/1). Numerical analysis in this work was undertaken on ARC4, part of the High Performance Computing facilities at the University of Leeds, UK.

Appendix A. Active medium description of the modelled QCLs

Structure 1

The exemplary GaAs/AlGaAs BTC THz QCL is designed for operation at a frequency of 2 THz [42]. Extraction from the lower laser level (LLL) to the injection laser level (ILL) is achieved through diagonal transitions within the miniband, while the ILL is within the mini band and is strongly coupled to the upper laser level (ULL) of the next period. The electronic structure of this device is illustrated in Fig. 10.

Structure 2

The exemplary InGaAs/InAlAs LO-phonon THz QCL is designed for high power operation [43]. Efficient extraction of the LLL is achieved by resonant LO phonon emission in the widest well of the structure. The material compositions are lattice matched to InP.

In Fig. 11 we show the bottom of the conduction band potential of the exemplary InGaAs/InAlAs LO-phonon THz QCL [43] with the wave functions squared shown.

Structure 3

The exemplary InGaAs/GaAsSb LO-phonon THz QCL is designed for high performance over a spectral emission range between 3.3 and 4 THz [44]. The material compositions are lattice matched to InP.

In Fig. 12 we show the bottom of the conduction band potential of the exemplary InGaAs/GaAsSb LO-phonon THz QCL [44] with the wave functions squared shown.

Structure 4

The exemplary GaSb/AlSb structure designed for pulsed operation at 2.6 THz [45]. The LLL is efficiently depopulated by electron-longitudinal optical phonon scattering into the ILL, which is located at an LO phonon

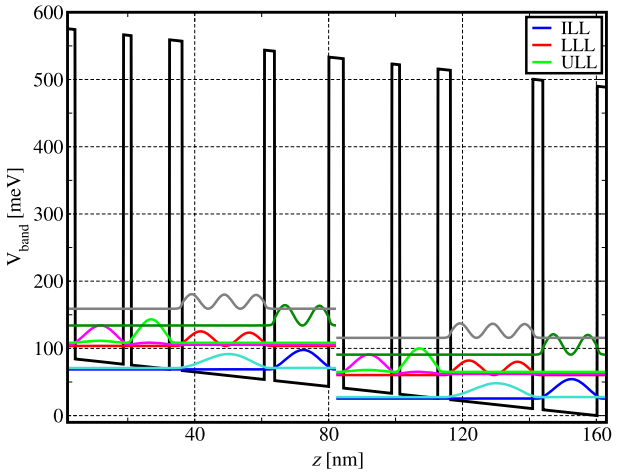

Fig. 13. Bottom of the conduction band potential of the exemplary GaSb/AlSb THz structure along with moduli squared of the corresponding wavefunctions [45]. The layer thicknesses, starting with the injection barrier are **4.3**/14.4/**2.4**/11.4/**3.8**/24.6/**3.0**/16.2 nm, where AlSb barriers are indicated in bold font, and the well layers are made of GaSb. The well doped to $1.9 \cdot 10^{16}$ cm^{-3} is underlined.

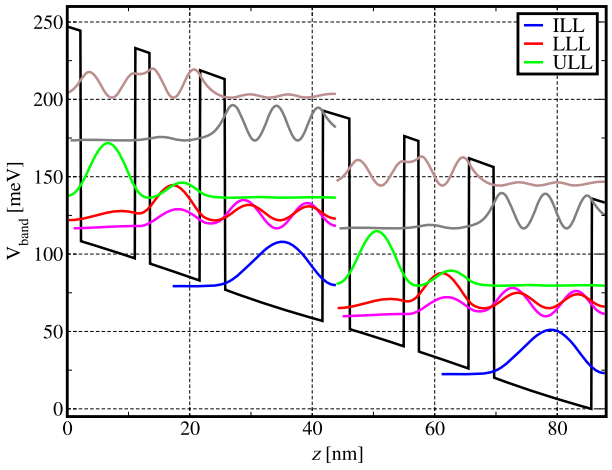

Fig. 14. Bottom of the conduction band potential of the exemplary GaAs/AlGaAs LO-phonon 200 K THz QCL along with moduli squared of the corresponding wavefunctions [61]. The layer thicknesses, starting with the injection barrier are **4.3**/8.9/**2.46**/8.15/**4.1**/(5.5+5.0+5.5) nm, where $Al_{0.15}Ga_{0.85}As$ barriers are indicated in bold font, and the middle part of the last well doped to $6.0 \cdot 10^{16}$ cm^{-3} is underlined.

energy (28.9 meV in GaSb) below the LLL and that is strongly coupled to the ULL of the next period. Resonant tunnelling occurs through the injection barrier depopulating the ILL.

In Fig. 13 we show the bottom of the conduction band potential of the exemplary GaSb/AlSb THz structure [45] with the wave functions squared shown.

Structure 5

The exemplary GaAs/AlGaAs LO-phonon QCL achieved pulsed operation at a high temperature of 200 K [61]. The LLL is efficiently depopulated by electron-longitudinal optical phonon scattering into the ILL, which is located at an LO phonon energy (36 meV in GaAs) below the LLL and that is strongly coupled to the ULL of the next period. Resonant tunnelling occurs through the injection barrier depopulating the ILL.

In Fig. 14 we show the bottom of the conduction band potential of the exemplary GaAs/AlGaAs LO-phonon 200 K THz QCL [61] with the wave functions squared shown.

Data availability

The data associated with this paper are openly available from the University of Leeds Data Repository at https://doi.org/10.5518/1639.

References

[1] H.A. Kramers, G.H. Wannier, Statistics of the two-dimensional ferromagnet. Part I, Phys. Rev. 60 (1941) 252.
[2] L.M. Walpita, Solutions for planar optical waveguide equations by selecting zero elements in a characteristic matrix, J. Opt. Soc. Am. A 2 (1985) 595–602.
[3] A. Ghatak, K. Thyagarajan, M. Shenoy, Numerical analysis of planar optical waveguides using matrix approach, J. Lightwave Technol. 5 (1987) 660–667.
[4] T. Makino, J. Glinski, Transfer matrix analysis of the amplified spontaneous emission of DFB semiconductor laser amplifiers, IEEE J. Quantum Electron. 24 (1988) 1507–1518.
[5] C.F. Fernandes, Transfer matrix modelling in DFB lasers, Microelectron. Eng. 43 (1998) 553–560.
[6] E.L. Adler, Matrix methods applied to acoustic waves in multilayers, IEEE Trans. Ultrason. Ferroelectr. Freq. Control 37 (1990) 485–490.
[7] C. Cai, G. Liu, K. Lam, A transfer matrix approach for acoustic analysis of a multilayered active acoustic coating, J. Sound Vib. 248 (2001) 71–89.
[8] H. Liu, J. Lee, Z. Cai, Analysis of nonlinear acoustoelastic effect of surface acoustic waves in laminated structures by transfer matrix method, Mech. Res. Commun. 31 (2004) 667–675.
[9] Z.Y. Li, L.L. Lin, Photonic band structures solved by a plane-wave-based transfer-matrix method, Phys. Rev. E 67 (2003) 046607.
[10] M.H. Eghlidi, K. Mehrany, B. Rashidian, Improved differential-transfer-matrix method for inhomogeneous one-dimensional photonic crystals, J. Opt. Soc. Am. B 23 (2006) 1451–1459.
[11] T. Zhan, X. Shi, Y. Dai, X. Liu, J. Zi, Transfer matrix method for optics in graphene layers, J. Phys. Condens. Matter 25 (2013) 215301.
[12] Y. Ando, T. Itoh, Calculation of transmission tunneling current across arbitrary potential barriers, J. Appl. Phys. 61 (1987) 1497–1502.
[13] B. Jonsson, S.T. Eng, Solving the Schrodinger equation in arbitrary quantum-well potential profiles using the transfer matrix method, IEEE J. Quantum Electron. 26 (1990) 2025–2035.
[14] E. Cassan, On the reduction of direct tunneling leakage through ultrathin gate oxides by a one-dimensional Schrödinger–Poisson solver, J. Appl. Phys. 87 (2000) 7931–7939.
[15] J.H. Davies, The Physics of Low-Dimensional Semiconductors: An Introduction, Cambridge university press, 1998.
[16] C. Jirauschek, Accuracy of transfer matrix approaches for solving the effective mass Schrödinger equation, IEEE J. Quantum Electron. 45 (2009) 1059–1067.
[17] N. Vukovic, J. Radovanovic, V. Milanovic, Enhanced modeling of band nonparabolicity with application to a mid-IR quantum cascade laser structure, Phys. Scr. 2014 (2014) 014014.
[18] T. Tu, G. Wang, X. Rui, Q. Zhou, Y. Miao, Direct differentiation method for sensitivity analysis based on transfer matrix method for multibody systems, Int. J. Numer. Methods Eng. 115 (2018) 1601–1622.
[19] J. Wang, X. Rui, B. He, X. Wang, K. Xie, A fast calculation method for sensitivity analysis based on multibody system transfer matrix method, Int. J. Appl. Mech. (2024).
[20] J. Wang, X. Rui, B. He, X. Wang, J. Zhang, K. Xie, Transfer matrix method for the analysis of multiple natural frequencies, Mathematics 12 (2024) 1413.
[21] R. Kazarinov, Possibility of amplification of electromagnetic waves in a semiconductor with superlattice, Sov. Phys. Semicond. 5 (1971) 707–709.
[22] J. Faist, F. Capasso, D.L. Sivco, C. Sirtori, A.L. Hutchinson, A.Y. Cho, Quantum cascade laser, Science 264 (1994) 553–556.
[23] R. Köhler, A. Tredicucci, F. Beltram, H.E. Beere, E.H. Linfield, A.G. Davies, D.A. Ritchie, R.C. Iotti, F. Rossi, Terahertz semiconductor-heterostructure laser, Nature 417 (2002) 156–159.
[24] B.S. Williams, Terahertz quantum-cascade lasers, Nat. Photonics 1 (2007) 517–525.
[25] C. Gmachl, F. Capasso, D.L. Sivco, A.Y. Cho, Recent progress in quantum cascade lasers and applications, Rep. Prog. Phys. 64 (2001) 1533.
[26] A.A. Kosterev, F.K. Tittel, Chemical sensors based on quantum cascade lasers, IEEE J. Quantum Electron. 38 (2002) 582–591.
[27] G. Wysocki, R. Lewicki, R.F. Curl, F.K. Tittel, L. Diehl, F. Capasso, M. Troccoli, G. Hofler, D. Bour, S. Corzine, R. Maulini, M. Giovannini, J. Faist, Widely tunable mode-hop free external cavity quantum cascade lasers for high resolution spectroscopy and chemical sensing, Appl. Phys. B 92 (2008) 305–311.
[28] J.B. McManus, J.H. Shorter, D.D. Nelson, M.S. Zahniser, D.E. Glenn, R.M. McGovern, Pulsed quantum cascade laser instrument with compact design for rapid, high sensitivity measurements of trace gases in air, Appl. Phys. B 92 (2008) 387.
[29] P. Dean, A. Valavanis, J. Keeley, K. Bertling, Y. Lim, R. Alhathlool, A. Burnett, L. Li, S. Khanna, D. Indjin, et al., Terahertz imaging using quantum cascade lasers—a review of systems and applications, J. Phys. D, Appl. Phys. 47 (2014) 374008.

[30] P. Dean, O. Mitrofanov, J. Keeley, I. Kundu, L. Li, E.H. Linfield, A. Giles Davies, Apertureless near-field terahertz imaging using the self-mixing effect in a quantum cascade laser, Appl. Phys. Lett. 108 (2016) 091113.
[31] A.D. Rakić, T. Taimre, K. Bertling, Y.L. Lim, P. Dean, D. Indjin, Z. Ikonić, P. Harrison, A. Valavanis, S.P. Khanna, M. Lachab, S.J. Wilson, E.H. Linfield, A.G. Davies, Swept-frequency feedback interferometry using terahertz frequency QCLs: a method for imaging and materials analysis, Opt. Express 21 (2013) 22194–22205.
[32] Y.L. Lim, T. Taimre, K. Bertling, P. Dean, D. Indjin, A. Valavanis, S.P. Khanna, M. Lachab, H. Schaider, T.W. Prow, et al., High-contrast coherent terahertz imaging of porcine tissue via swept-frequency feedback interferometry, Biomed. Opt. Express 5 (2014) 3981–3989.
[33] G. Bastard, Superlattice band structure in the envelope-function approximation, Phys. Rev. B 24 (1981) 5693.
[34] G. Bastard, Theoretical investigations of superlattice band structure in the envelope-function approximation, Phys. Rev. B 25 (1982) 7584.
[35] G. Bastard, Wave Mechanics Applied to Semiconductor Heterostructures, John Wiley and Sons Inc., New York, NY (USA), 1990.
[36] C. Sirtori, F. Capasso, J. Faist, S. Scandolo, Nonparabolicity and a sum rule associated with bound-to-bound and bound-to-continuum intersubband transitions in quantum wells, Phys. Rev. B 50 (1994) 8663.
[37] U. Ekenberg, Nonparabolicity effects in a quantum well: sublevel shift, parallel mass, and Landau levels, Phys. Rev. B 40 (1989) 7714.
[38] J. Cooper, A. Valavanis, Z. Ikonić, P. Harrison, J. Cunningham, Finite difference method for solving the schrödinger equation with band nonparabolicity in mid-infrared quantum cascade lasers, J. Appl. Phys. 108 (2010).
[39] A. Demić, J. Radovanović, V. Milanović, Analysis of the influence of external magnetic field on transition matrix elements in quantum well and quantum cascade laser structures, Superlattices Microstruct. 96 (2016) 134–149.
[40] S. Yu, K. Kim, M.A. Stroscio, G. Iafrate, J.-P. Sun, G.I. Haddad, Transfer matrix method for interface optical-phonon modes in multiple-interface heterostructure systems, J. Appl. Phys. 82 (1997) 3363–3367.
[41] F. Alharbi, An explicit FDM calculation of nonparabolicity effects in energy states of quantum wells, Opt. Quantum Electron. 40 (2008) 551–559.
[42] A. Demić, A. Grier, Z. Ikonić, A. Valavanis, C.A. Evans, R. Mohandas, L. Li, E.H. Linfield, A.G. Davies, D. Indjin, Infinite-period density-matrix model for terahertz-frequency quantum cascade lasers, IEEE Trans. Terahertz Sci. Technol. 7 (2017) 368–377.
[43] C. Deutsch, M.A. Kainz, M. Krall, M. Brandstetter, D. Bachmann, S. Schoonhuber, H. Detz, T. Zederbauer, D. MacFarland, A.M. Andrews, et al., High-power growth-robust InGaAs/InAlAs terahertz quantum cascade lasers, ACS Photonics 4 (2017) 957–962.
[44] C. Deutsch, M. Krall, M. Brandstetter, H. Detz, A. Andrews, P. Klang, W. Schrenk, G. Strasser, K. Unterrainer, High performance InGaAs/GaAsSb terahertz quantum cascade lasers operating up to 142 K, Appl. Phys. Lett. 101 (2012).
[45] H. Yasuda, I. Hosako, S. Miyashita, M. Patrashin, GaSb/AlSb quantum cascade laser for terahertz signal source, in: 2005 Asia-Pacific Microwave Conference Proceedings, vol. 5, IEEE, 2005, p. 3.
[46] M. Braun, U. Rossler, Magneto-optic transitions and non-parabolicity parameters in the conduction band of semiconductors, J. Phys. C, Solid State Phys. 18 (1985) 3365.
[47] V. Golubev, V. Ivanov-Omskii, I. Minervin, A. Osutin, D. Polyakov, Nonparabolicity and anisotropy of the electron energy spectrum in GaAs, Zh. Èksp. Teor. Fiz. 88 (1985) 2052–2062.
[48] J.-M. Jancu, R. Scholz, E.d.A. e Silva, G. La Rocca, Atomistic spin-orbit coupling and k·p parameters in III-V semiconductors, Phys. Rev. B 72 (2005) 193201.
[49] N. Vuković, V. Milanović, J. Radovanović, Influence of nonparabolicity on electronic structure of quantum cascade laser, Phys. Lett. A 378 (2014) 2222–2225.
[50] J. Demmel, I. Dumitriu, O. Holtz, Fast linear algebra is stable, Numer. Math. 108 (2007) 59–91.
[51] A. Lucas, E. Kartheuser, R. Badro, Electron-phonon interaction in dielectric films. Application to electron energy loss and gain spectra, Phys. Rev. B 2 (1970) 2488.
[52] J.J. Licari, R. Evrard, Electron-phonon interaction in a dielectric slab: Effect of the electronic polarizability, Phys. Rev. B 15 (1977) 2254.
[53] K. Kim, M. Stroscio, Electron-optical-phonon interaction in binary/ternary heterostructures, J. Appl. Phys. 68 (1990) 6289–6292.
[54] H. Teng, J. Sun, G.I. Haddad, M.A. Stroscio, S. Yu, K. Kim, Phonon assisted intersubband transitions in step quantum well structures, J. Appl. Phys. 84 (1998) 2155–2164.
[55] H. Xiao-Yong, C. Jun-Cheng, L. Jing-Tao, F. Song-Lin, Simulation of confined and interface phonons scattering in terahertz quantum cascade laser, Chin. Phys. Lett. 22 (2005) 3163.
[56] N. Mori, T. Ando, Electron–optical-phonon interaction in single and double heterostructures, Phys. Rev. B 40 (1989) 6175.
[57] L. Wendler, Electron–phonon interaction in dielectric bilayer systems. effect of the electronic polarizability, Phys. Status Solidi B 129 (1985) 513–530.
[58] R. Chen, D. Lin, T.F. George, Optical-phonon modes in a double heterostructure of polar crystals, Phys. Rev. B 41 (1990) 1435.
[59] S. Adachi, GaAs, AlAs, and $Al_xGa_{1-x}As$: Material parameters for use in research and device applications, J. Appl. Phys. 58 (1985) R1–R29.
[60] M.A. Stroscio, M. Dutta, Phonons in nanostructures, Cambridge University Press, 2001.
[61] S. Fathololoumi, E. Dupont, C. Chan, Z. Wasilewski, S. Laframboise, D. Ban, A. Mátyás, C. Jirauschek, Q. Hu, H. Liu, Terahertz quantum cascade lasers operating up to 200 k with optimized oscillator strength and improved injection tunneling, Opt. Express 20 (2012) 3866–3876.
[62] P. Harrison, A. Valavanis, Quantum Wells, Wires and Dots: Theoretical and Computational Physics of Semiconductor Nanostructures, John Wiley & Sons, 2016.
[63] X. Gao, D. Botez, I. Knezevic, Phonon confinement and electron transport in GaAs-based quantum cascade structures, J. Appl. Phys. 103 (2008).